

Understanding and Eliminating the Large-kernel Effect in Blind Deconvolution

Li Si-Yao, Qian Yin*, and Ping Guo, *Senior Member, IEEE*

Abstract—Blind deconvolution consists of recovering a clear version of an observed blurry image without specific knowledge of the degradation kernel. The kernel size, however, is a required hyper-parameter that defines the range of the support domain. In this study, we experimentally and theoretically show how large kernel sizes introduce noises to expected zeros in the kernel and yield inferior results. We explain this effect by demonstrating that sizeable kernels lower the squares cost in optimization. We also prove that this effect persists with a probability of one for noisy images. Using 1D simulation, we quantify the increment of error of estimated kernel with its size. To eliminate this effect, we propose a low-rank based penalty that reflects structural information of the kernel. Compared to the generic ℓ_α , our penalty can respond to even a small amount of random noise in the kernel. Our regularization reduces the noise and efficiently enhances the success rate of large kernel sizes. We also compare our method to state-of-art approaches and test it using real-world images.

Index Terms—image deblurring, blind deconvolution, kernel size, regularization.

I. INTRODUCTION

Blind deconvolution methods are to recover a latent clear version from an observed blurry image without knowing the degradation kernel. The model of image blur is

$$y = x * k + n, \quad (1)$$

where y is the blurred image, x is the latent clear one, k is the kernel (a.k.a. Point Spread Function (PSF)) and n represents random Gaussian noise produced during photographing.

One popular approach is to maximize the posterior (MAP) $p(x, k|y)$ and reformulate the problem into a regularized least squares optimization [1]:

$$(\hat{x}, \hat{k}) = \arg \min_{x, k} (\|x * k - y\|^2 + \lambda g(x) + \sigma h(k)) \quad (2)$$

where g and h are prior function designed to prefer sharp images and ideal kernels respectively. This two-variable optimization is implemented as two alternate sub-steps:

$$\hat{x}^{(i+1)} = \arg \min_x (\|x * \hat{k}^{(i)} - y\|^2 + \lambda g(x)) \quad (3)$$

and

$$\hat{k}^{(i+1)} = \arg \min_k (\|\hat{x}^{(i+1)} * k - y\|^2 + \sigma h(k)). \quad (4)$$

Although k is unknown, most implementations require kernel size as a manually tuned hyper-parameter that limits the support domain. The improper selection of kernel size yields inferior results in MAP methods. When the preset kernel size is too small, there will not be enough room for \hat{k} to expand during iterations, which yields high errors of recovered images. Contrastively, when kernel size is greater than ground truth, MAP methods also yield inferior results. This phenomenon was firstly mentioned by Fergus *et al.* [2]. Similarly, Cho and Lee [3] showed that the residue cost of (2) increases with kernel size when k is larger than the proper one. To show this effect clearly we tested our implementation described in Section 4 (but set μ and σ zero) using one-half to three times the truth size iteratively. Figure 1(d-f) shows that the larger the kernel size than ground truth the poorer the deblurred image. At the same time, kernels become more noisy with higher numerical errors. Figure 1(b) shows both the error ratio of restored images and the Sum of Squared Difference (SSD) of estimated kernels reach the lowest around the truth size and increase afterwards.

It should be noted here that in this experiment, we omitted regularization h , hence the k-step equals to a bare least squares problem:

$$\hat{k}^{(i+1)} = \arg \min_k \|\hat{x}^{(i+1)} * k - y\|^2. \quad (5)$$

We also avoided using multi-scaling scheme and threshold in this experiment. Parameters that performed well on the truth size were kept identical for larger sizes during the experiment.

In this study, to explore the source of this effect, we transfer convolution parts of (3) and (4) to affine transformations and analyse their properties on kernel size. We show that for x in sparse distributions of clear images, this large-kernel effect remains with probability 1. Further, we simulate and quantify how the error increases with kernel size.

Ideal kernels are regarded to be sparse. A variety of generic sparsity regularizations are used on k in the literature. The most popular choice is ℓ_2 norm [4]–[7], taking advantage of the convenience of optimization. Some other implementations used ℓ_1 norm [8]–[10] while Zuo *et al.* [11] used the hyper-Laplacian prior (ℓ_α with $0 < \alpha < 1$) to maintain the sparsity of the estimated kernel. However, previous works generally treated regularization h as an accessory of the success of MAP methods, e.g., Perrone and Favaro [12] omitted h directly. The literature lacks a targeted discussion on the selection of kernel

This work is funded by National Natural Science Foundation of China (NSFC) (61472043, 61375045) and Joint Research Fund in Astronomy under cooperative agreement between the National Natural Science Foundation of China (NSFC) and Chinese Academy of Sciences (CAS) (U1531242).

Li Si-Yao and Q. Yin are with the College of Information Science and Technology, Beijing Normal University, Beijing, 100875 CN (e-mail: lisiyao@mail.bnu.edu.cn, yinqian@bnu.edu.cn).

Ping Guo is with the School of System Science, Beijing Normal University, Beijing, 100875, CN (email: pguo@ieee.org).

*Q. Yin is the corresponding author.

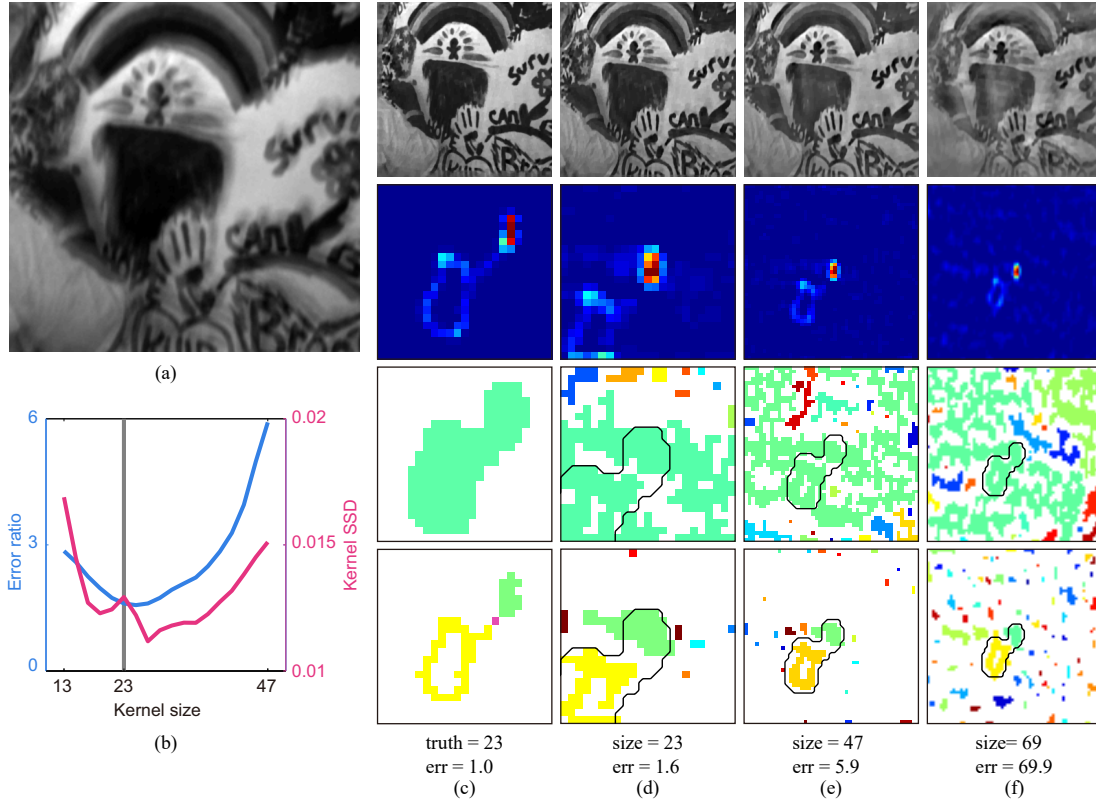


Fig. 1. Large kernels produce inferior results. (a) The blurry image. (b) The numerical errors on kernel size. (c-f) Deblurred results: in the first row are restored images; in the second row are corresponding estimated kernels; in the third row are the support domains ($k > 0$); in the last row are the domains of $k > \max(k)/30$, where adjacent positive pixels are colored identically and zeros are white.

regularization. In this study, we take a novel regularization targeting to reduce the noise in \hat{k} and eliminate the unwanted effect yielded by large kernels.

In addition to the regularization, operations after the k -step also enhance the quality of the estimated kernel. Cho and Lee [6] removed any elements smaller than $1/20$ of the maximum of \hat{k} to purify the estimated kernel. Xu and Jia [4] proposed an iterative support domain detector based on the differences of elements of \hat{k} . Beyond various refinements, two constraints of k are widely recognized: (i) the sum of k equals 1 and (ii) the elements of k are no smaller than 0. With respect to (i), Kundur *et al.* [13] indicates that the mean of a clear image is preserved in the blurry; Levin *et al.* [14] emphasizes that the normalization prevents scaling conflicts. For (ii), the PSF is naturally greater than zero because the contribution of light is positive. These constraints are realized as projections after the k -step [8], [11]. Perrone and Favaro [12] showed that projections after alternate Gradient Descent prevent the trivial (delta) solution using 1D simulations.

II. ANALYSIS

Before analysing the source of larger-kernel effect, we firstly introduce an interesting fact that we call *Plumping Effect*.

Theorem 1. (Plumping Effect) Let $A = [v_1 \dots v_n]$, where $v_i \in \mathbb{R}^m$ ($m \geq n + 1$). Let $B = [w_1 A w_2]$ where $w_1, w_2 \in \mathbb{R}^m$ and $\text{rank}(B) > \text{rank}(A)$. Given an m -D random vector

b whose elements are i.i.d. with the continuous probability density function p , for $u \in \mathbb{R}^m$

$$\Pr(\inf\{\|Bu - b\|^2\} < \inf\{\|Au - b\|^2\}) = 1.$$

Proof.

$$\begin{aligned} & \Pr(\inf\{\|Bu - b\|^2\} \geq \inf\{\|Au - b\|^2\}) \\ &= \Pr(b \in \mathbb{R}^m \setminus \text{span}\{w_1, w_2\}) \\ &= \int_{\Omega} dp(b) \end{aligned}$$

where $\Omega = \mathbb{R}^m \setminus \text{span}\{w_1, w_2\}$. For w_1, w_2 are linear independent to $\{v_1, \dots, v_n\}$, we have $w_1 \neq 0$ or $w_2 \neq 0$. Hence, the Lebesgue measure of Ω is zero, and the probability is zero. \square

Theorem 1 shows that padding linear independent columns to a thin matrix yields lower residue cost; hence the least squares solution will change.

The degradation (convolution) part in (1) is equivalent to linear transformations:

$$x * k = T_k x = T_x k. \quad (6)$$

where $x, y \in \mathbb{R}^{M \times N}$, $k \in \mathbb{R}^{L \times K}$; T_k and T_x are blocked banded Toeplitz matrices [15], [16]; $T_k \in \mathbb{R}^{MN \times MN}$ and $T_x \in \mathbb{R}^{MN \times LK}$; \underline{A} represents the column-wise expanded vector of matrix A ; L and K are required to be odd.

Dimensions of T_k will not change with kernel size. Especially, T_k remains the same when L and K increase by wrapping a layer of zeros around k . The result of the x -step keeps the same if \hat{k} expanded by zero padding, hence the x -step should not be blamed as the source of the large-kernel effect. In contrast, when k is larger, T_x will become plumper for the same x . In 1D cases, where $N = K = 1$, assume $L = 2l + 1$, then

$$\begin{aligned}
 T_x(L) &= \begin{bmatrix} x_{l+1} & \cdots & x_2 & x_1 & 0 & \cdots & 0 \\ \vdots & & \vdots & x_2 & x_1 & \ddots & \vdots \\ x_{M-1} & & \vdots & \vdots & x_2 & \ddots & 0 \\ x_M & \ddots & \vdots & \vdots & \vdots & \ddots & x_1 \\ 0 & \ddots & x_{M-1} & \vdots & \vdots & \ddots & x_2 \\ \vdots & \ddots & x_M & x_{M-1} & \vdots & \ddots & \vdots \\ 0 & \cdots & 0 & x_M & x_{M-1} & \cdots & x_{M-l} \end{bmatrix} \\
 &= [J^{(-l)}\mathbf{x} \cdots J^{(-1)}\mathbf{x} \mathbf{x} J^{(1)}\mathbf{x} \cdots J^{(l)}\mathbf{x}].
 \end{aligned} \tag{7}$$

During blind deconvolution iterations, for identical values of $\hat{\mathbf{x}}^{(i)}$, a larger L introduces a greater number of columns onto both sizes of $T_{\hat{\mathbf{x}}^{(i)}}$ and results in different solutions. To illustrate this point, we tested a 1D version of blind deconvolution without kernel regularization and took different values of L (truth and double and four times the truth size) for the 50th k -step optimization after 49 truth-size iterations (see Figure 2). Figure 2(a-c) show that the optimal solutions in different sizes differ slightly on the main body that lies within the ground truth size (colored in red), but greatly outside this range (colored in green), where zeros are expected. Figure 2(d-f) compare ground truth to estimated kernels in (a-c) after nonnegativity and sum-to-one projections. Larger sizes yield a greater number of positive noises; hence, they lower the weight of the main body after the projection and change the outlook of kernel.

Even if $\hat{\mathbf{x}}^{(i)}$ successfully iterates to truth \mathbf{x} , Theorem 1 implicates the large-kernel effect remains for random Gaussian noise \mathbf{n} . We now show

$$\Pr(\text{rank}(T_x(L+2)) > \text{rank}(T_x(L))) = 1, \tag{8}$$

which is the condition of the *Plumping Effect*. Firstly, we have

$$\begin{aligned}
 &\Pr(\text{rank}(T_x(L+2)) > \text{rank}(T_x(L))) \\
 &\geq \Pr(\text{rank}(T_x(M)) = M).
 \end{aligned} \tag{9}$$

Kaltfofen and Lobo [17] proved that for an M -by- M Toeplitz matrix composed of finite field of q elements,

$$\Pr(\text{rank}(T_{M \times M}) = M) = 1 - 1/q. \tag{10}$$

In our case, clear images have statistical sparsity on derivative fields [18], [19], and elements of \mathbf{x} are modeled to be continuous in hyper-Laplacian distributions [20]:

$$p(\mathbf{x}_j) = \begin{cases} \beta \exp(-\gamma|\mathbf{x}_j|^\alpha) & \mathbf{x}_j \in [-1, 1] \\ 0 & \text{otherwise.} \end{cases} \tag{11}$$

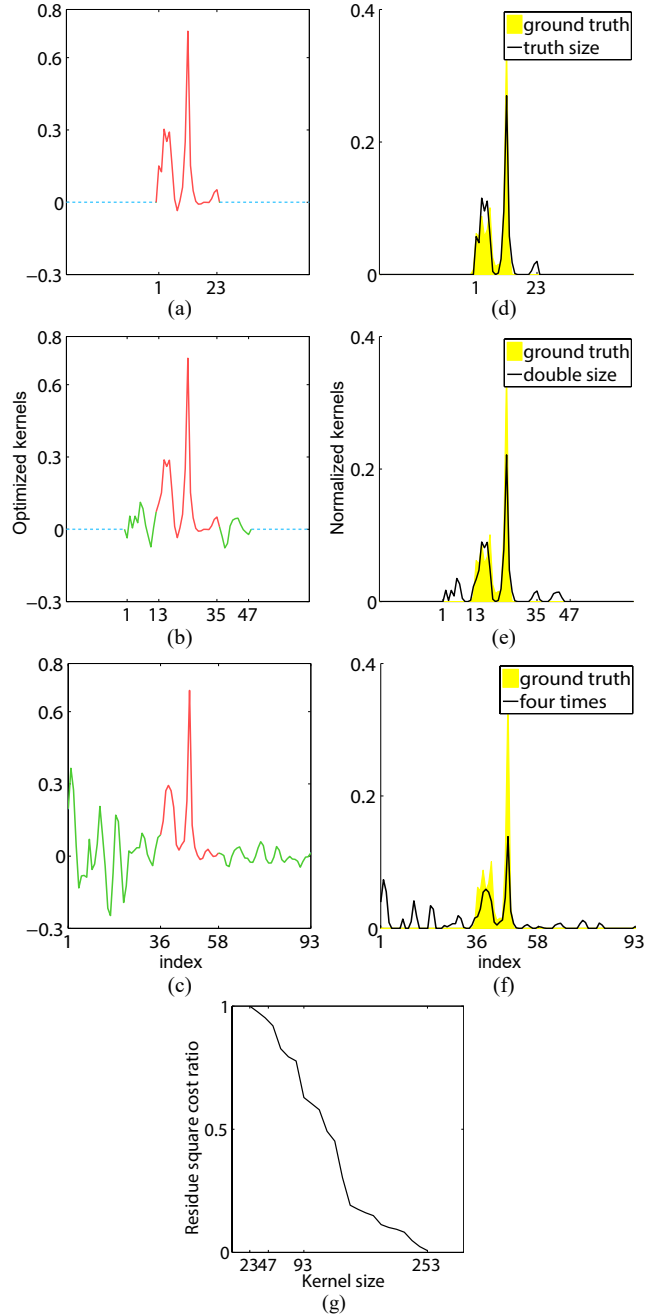


Fig. 2. The estimated kernels in 1D Blind deconvolution simulations. (a-c) are optimized kernels of different sizes after the 50th iteration. (d-f) are corresponding normalized kernels to left after nonnegativity and sum-to-one projections. (g) shows the residue squares cost of (5) of the optimized kernel on its size. In this experiment, \mathbf{x} is a 255×1 vector extracted from a real image and the truth \mathbf{k} is generated by column-wisely adding a 23×23 truth kernel from Levin's dataset [14]. The signal prior is $\frac{\ell_1}{\ell_2}$. This figure is recommended to view in color.

Then we have

Theorem 2.

$$\Pr(\text{rank}(T_x(M)) = M) = 1.$$

Proof. See Appendix A. \square

Theorem 1 implicates that the larger the kernel size the

greater the error of k due to noise n . We now quantify this increment.

Assume \hat{x} iterates to ground truth x_{gt} during iterations, then, for the estimated kernel, we have

$$\begin{aligned}\hat{k} &= \arg \min_k \|T_{x_{gt}} k - \underline{y}\|^2 \\ &= \arg \min_k \|T_{x_{gt}} k - T_{x_{gt}} k_{gt} - \underline{n}\|^2 \\ &= \underline{k}_{gt} + \arg \min_k \|T_{x_{gt}} k - \underline{n}\|^2 \\ &= \underline{k}_{gt} + T_{x_{gt}}^\dagger \underline{n}\end{aligned}\quad (12)$$

where A^\dagger represents Moore-Penrose pseudoinverse of matrix A . Then

$$SSD = \|\hat{k} - k_{gt}\|^2 = \|T_{x_{gt}}^\dagger \underline{n}\|^2. \quad (13)$$

Assume $\|n\| = 1$, then

$$s_1(T_{x_{gt}}^\dagger) \leq \|T_{x_{gt}}^\dagger \underline{n}\| \leq s_n(T_{x_{gt}}^\dagger), \quad (14)$$

where s_1 and s_n represent smallest and largest singular values. Equivalently, we have

$$\frac{1}{s_n(T_{x_{gt}})} \leq \|T_{x_{gt}}^\dagger \underline{n}\| \leq \frac{1}{s_1(T_{x_{gt}})}. \quad (15)$$

Based on [21], [22], for arbitrary matrix $A = [\mathbf{a}_1, \mathbf{a}_2, \dots, \mathbf{a}_d]$, we have

$$\frac{\text{height}(\mathbf{a}_1, \mathbf{a}_2, \dots, \mathbf{a}_d)}{\sqrt{d}} \leq s_1(A) \quad (16)$$

and

$$s_n(A) \leq \sqrt{d} \max_i \|\mathbf{a}_i\|. \quad (17)$$

For arbitrary $A = T_x(L)$, $\max_i \|\mathbf{a}_i\| = \|x\| \leq \sqrt{M}$. Hence,

$$\frac{1}{\sqrt{ML}} \leq \|T_x^\dagger \underline{n}\| \leq \frac{\sqrt{L}}{\text{height}(J^{(-l)}x, \dots, x, \dots, J^{(l)}x)}. \quad (18)$$

Function *height* will decrease when L grows, because more linear independent columns are introduced into A . To quantify this decrement, we simulated 100 times, in each of which we generated random x with length $M = 254$ and PDF as in (11) with $\gamma = 10$ and $\alpha = 0.5$. Figure 3(b) shows the decreasing mean and standard deviation of simulated heights on L . Using this simulated data, we plotted the lower and upper bound of $\|T_x^\dagger \underline{n}\|$ based on (18). We also extracted a line x_{ex} from a clear image of Levin's set [14], generated a normalized random vector \underline{n} and compared $\|T_{x_{ex}} \underline{n}\|$ to theoretical boundaries. Figure 3(c) shows the error increases hyper-linearly.

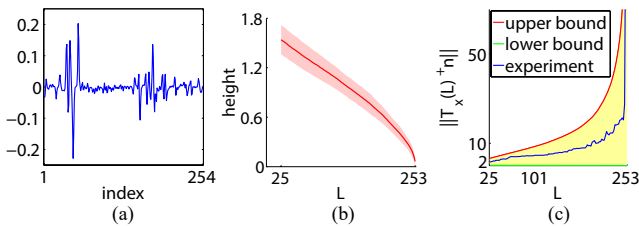


Fig. 3. (a) The extracted row from a clear image. (b) The mean and standard deviation of simulated heights. (c) Theoretical bounds using (b) and experimental result of (a).

During blind deconvolution iterations, implicit noise [9] occurs when $\hat{x} \neq x_{gt}$. Cho and Lee [3] indicated that \hat{x} should be regarded as a sparse approximation to x_{gt} . Assume $\hat{x} = x_{gt} + \Delta x$ and $n = 0$, then

$$\begin{aligned}\hat{x} * k_{gt} &= x_{gt} * k_{gt} + \Delta x * k_{gt} \\ &= x_{gt} * k_{gt} + n_{\Delta x},\end{aligned}\quad (19)$$

and

$$\begin{aligned}\hat{k} &= \arg \min_k \|T_{\hat{x}} k - \underline{y}\|^2 \\ &= \arg \min_k \|(T_{x_{gt}} + T_{\Delta x})k - T_{x_{gt}} k_{gt}\|^2 \\ &= (T_{x_{gt}} + T_{\Delta x})^\dagger T_{x_{gt}} k_{gt}.\end{aligned}\quad (20)$$

Then

$$SSD = \|(T_{x_{gt}} + T_{\Delta x})^\dagger T_{x_{gt}} - I\| k_{gt}\|^2. \quad (21)$$

To quantify how singular values of $(T_{x_{gt}} + T_{\Delta x})^\dagger T_{x_{gt}} - I$ changes with kernel size, we simulated 100 times, in each of which we generated random x with length 254 and PDF in (11) with $M = 254$, $\gamma = 10$ and $\alpha = 0.5$, and generated random Gaussian vector Δx where $\|\Delta x\| = \|x\|/100$. Figure 4(a) shows one example of generated x and Δx . Figure 4(b) shows means and standard deviations of s_1 , s_n and \bar{s} of simulated $(T_x + T_{\Delta x})^\dagger T_x - I$ on L , respectively. The error of \hat{k} is expected to grow with kernel size even $n = 0$.

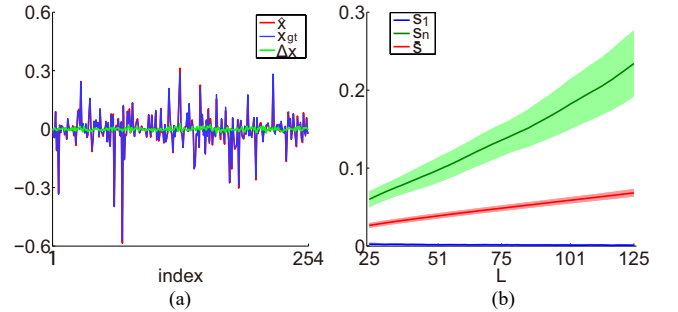


Fig. 4. (a) Simulated sparse signal examples. (b) Simulated singular values of $(T_x + T_{\Delta x})^\dagger T_x - I$.

III. LOW-RANK REGULARIZATION

The large-kernel effect is yielded by noise in ultra-sized kernels. Figure 1 and Figure 2 show that main bodies of kernels are kept but noise take greater amounts when kernel is larger. To constrain \hat{k} to be ideally clean, regularization h is expected to distinguish noise from clean kernels efficiently.

To eliminate the noise in kernel, we take low-rank regularization on k such that (4) becomes

$$\hat{k}^{(i+1)} = \arg \min_k \left(\|\hat{x}^{(i+1)} * k - y\|^2 + \sigma \text{rank}(k) \right). \quad (22)$$

Because the direct rank optimization is an NP-hard problem, continuous proximal functions are required. Fazel *et al.* [23] proposed

$$\log \det((X + \delta I)) \quad (23)$$

as a heuristic proxy for $X \in \mathbb{S}_+^N$ where I is the N-by-N identity matrix and δ is a small positive number. A 1D case is shown in Figure 3.

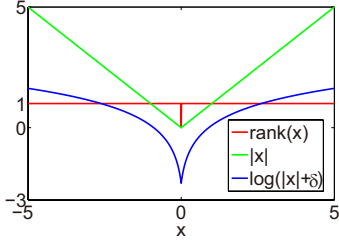


Fig. 5. 1D demonstration of the rank function, the nuclear norm and log det.

To allow this approximation to play a role in general matrices, the low-rank object is substituted to $(XX^T)^{1/2}$ [24]. The regularization function then becomes

$$h(X) = \log \det((XX^T)^{1/2} + \delta I) = \sum_j \log(s_i + \delta) \quad (24)$$

where s_i is the i -th singular value of X .

The motivation to take low-rank regularization on k is based on a common phenomenon of noise matrices. Figure 4(a-b) shows a nonnegativity projected Gaussian noise matrix and its singular values in decreasing order. For a noise matrix, where light and dark alternate irregularly, the distribution of singular values decays sharply at lower indices, then it breaks and drag a relatively long and flat tail to the last. This phenomenon is generic [15]. Based on this fact, noise matrices

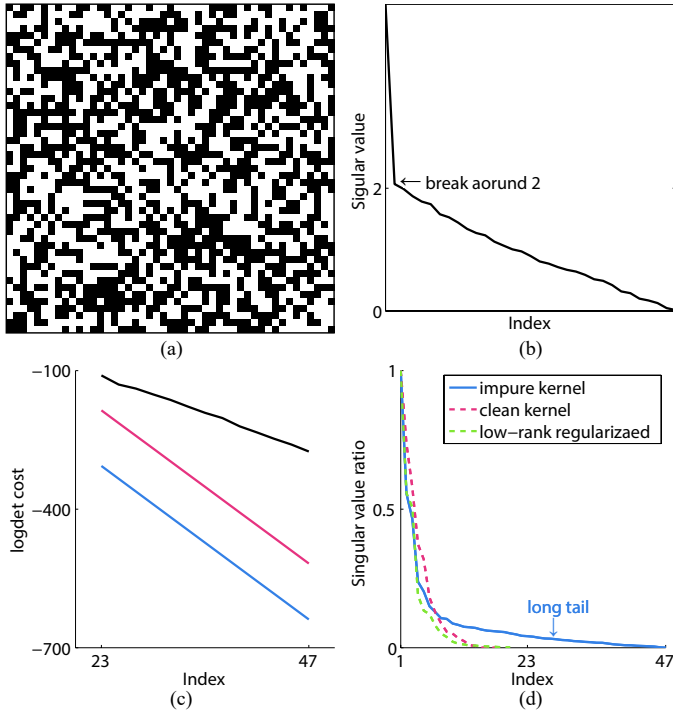


Fig. 6. Singular values of clean kernels and noisy matrices. (a) shows the support domain (black) of a 47×47 random Gaussian noise matrix after nonnegativity projection. (b) is the distribution of singular values of (a). In (c) we compare the log det cost of random Gaussian noise matrix (black), the truth kernel from [14] after zero-padding (red), and the Gaussian PSF with size/6 standard deviation (blue) on kernel size. In (d) we compare the distribution of scaled singular values (the maximum to 1) of clean, impure and regularized kernels. This figure is recommended to view in color.

are distinguished by high log det cost from real kernels (see Figure 4(c)). Figure 4(d) shows that singular values of low-rank regularized kernel are distributed similarly as ground truth, compared with the impure one.

Compared to previously used ℓ_α norms, low-rank regularization responds more efficiently to noise. To illustrate this point, we generated a noisy kernel by adding a small percentage (ϵ) of Gaussian noise and $1 - \epsilon$ of the real kernel. Figure 5 shows that the low-rank cost rapidly adjust favorably to the noise but ℓ_α norms fail. That is because ℓ_α only takes statistical information. An extrem example consists of disrupting a truth kernel and randomly reorganizing its elements, with ℓ_α cost unchanged. In contrast, rank (singular values) corresponds to structural information of a matrix.

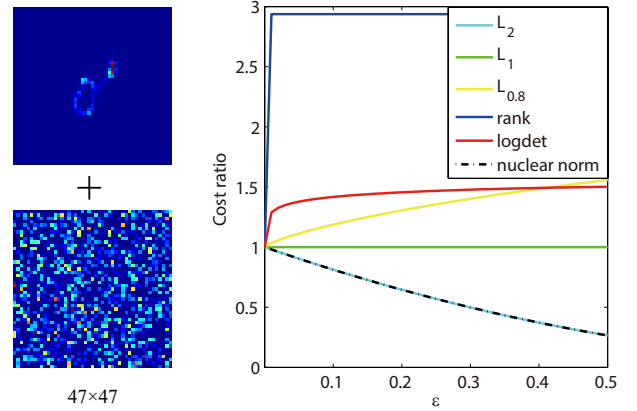


Fig. 7. Comparison on respond to noise. The cost ratio is calculated as $1 + \frac{\text{cost}(\epsilon) - \text{cost}(0)}{|\text{cost}(0)|}$. This figure is recommended to view in color.

IV. IMPLEMENTATION

A. Updating k

It should be firstly noted that the log det function is non-convex (it is actually concave on \mathbb{S}_+). To solve the low-rank regularized least squares problem 4 with h defined in (24), we introduce the auxiliary variable $\Psi = k$ and reformulate the optimization into

$$\begin{aligned} \min_{k, \Psi} & \left(\|x^{(i+1)} * \Psi - y\|^2 + \sigma \log \det \left((kk)^{\frac{1}{2}} + \delta I \right) \right) \\ \text{s.t. } & \Psi = k \end{aligned} \quad (25)$$

Using the Lagrange method, (25) is solved by two alternate sub-optimizations

$$\begin{cases} \hat{\Psi}^{(j+1)} = \arg \min_{\Psi} \left(\|\hat{x}^{(i+1)} * \Psi - y\|^2 + \mu \|\Psi - \hat{k}^{(j)}\|^2 \right) \\ \hat{k}^{(j+1)} = \arg \min_k \left(\frac{1}{2\tau} \|k - \hat{\Psi}^{(j+1)}\|^2 + \sigma h(k) \right) \end{cases} \quad (26)$$

where j is the iteration number while μ and τ are trade-off parameters.

The Ψ -substep is convex and accomplished using the Conjugate Gradient method. For k -substep, the requirement for low rank is limited; otherwise, the regularization may change the

Algorithm 1 Updating k with low-rank regularization

Input: $x, y, \mu, \tau, OuterIterMax, CGIterMax, innerIterMax$
Output: \hat{k}

```

1: for  $j \leftarrow 0$  to  $OuterIterMax - 1$  do
2:   if  $j = 0$  then
3:      $\hat{\Psi}^{(j+1)} \leftarrow \min_{\Psi} \|x * \Psi - y\|^2$  using CG with
       maximum  $CGIterMax$  iterations
4:   else
5:      $\mu^{(j)} = \mu (e^j / e^{OuterIterMax})$ 
6:      $\hat{\Psi}^{(j+1)} \leftarrow \min_{\Psi} (\|x * \Psi - y\|^2 + \mu^{(j)} \|\Psi - k^{(j)}\|^2)$ 
       using CG with maximum  $CGIterMax$  iterations
7:   end if
8:   Initializing  $k^{(0)}$  with all singular values equal to 1
9:   for  $t \leftarrow 0$  to  $innerIterMax - 1$  do
10:     $k^{(t+1)} \leftarrow \text{prox}_{\tau h_{k^{(t)}}}(\hat{\Psi}^{(j)})$ 
11:   end for
12:    $\hat{k}^{(j+1)} \leftarrow \max\{k^{(innerIterMax)}, 0\}$ 
13:    $\hat{k}^{(j+1)} \leftarrow \hat{k}^{(j+1)} / \sum \hat{k}^{(j+1)}$ 
14: end for
15:  $\hat{k} \leftarrow \hat{k}^{(outerIterMax)}$ 

```

main body of kernel—an extreme result is $\hat{k} = 0$. Thus, our strategy is to lower the rank at $\hat{\Psi}$ locally. Using the first-order Taylor expansion of h at fixed matrix Z :

$$\begin{aligned}
h_Z(X) &= h(Z) \\
&\quad + \text{tr} \left((ZZ^T)^{\frac{1}{2}} + \delta I \right)^{-1} \left((XX^T)^{\frac{1}{2}} - (ZZ^T)^{\frac{1}{2}} \right) \\
&= h(Z) + \sum_i \frac{s_i - \hat{s}_i}{\hat{s}_i + \delta}
\end{aligned} \tag{27}$$

where \hat{s}_i is the i -th eigenvalue of Z , the k -substep is transformed into an iterative optimization

$$k^{(t+1)} = \arg \min_k \left(\frac{1}{2\tau} \|k - \hat{\Psi}^{(j+1)}\|^2 + \sigma h_{k^{(t)}}(k) \right) \tag{28}$$

where t is the inner iteration number. For convenience we set σ as a flag (if $\sigma = 0$, the k -substep will be skipped) and only tuned τ as the trade-off parameter.

Define the proximal mapping of function ϕ as follows:

$$\text{prox}_{\phi}(v) = \arg \min_u \left(\frac{1}{2} \|u - v\|^2 + \phi(u) \right). \tag{29}$$

Dong *et al.* [24] proved that one solution to the proximal mapping of τh_Z is

$$\text{prox}_{\tau h_Z}(X) = U (\Sigma - \tau \text{diag}(w))_+ V^T \tag{30}$$

where $U \Sigma V^T$ is SVD of X , $w_i = 1/(\hat{s}_i + \delta)$ and $(A)_+ = \max\{A, 0\}$. Local low-rank optimization is iteratively implemented via the given parameter τ (see Algorithm 1).

It should be noted here that μ is designed to exponentially grow with j to allow more freedom of $\hat{\Psi}$ for early iterations.

B. Updating x

As ℓ_α norms prefer the blurry images [12], [14], we take $g = \ell_1/\ell_2$ in this work, as proposed by Krishnan *et al.* [8]. The

non-convex ℓ_1/ℓ_2 regularized least squares problem is solved by fixing ℓ_2 . Hence, the problem is transformed into a linear optimization problem

$$\min_x (\|x * k - y\|^2 + \lambda' \|x\|_1) \tag{31}$$

and is solved by iteratively minimizing a convex envelope (for step η small enough) equivalent to

$$x^{(t+1)} = \text{prox}_{\eta \lambda \|x\|_1} \left(u^{(t)} \right) = \text{sgn}(u^{(t)}) (|u^{(t)}| - \eta \lambda)_+ \tag{32}$$

where $u^{(t)} = x^{(t)} - \eta [\nabla_x \|x * k - y\|^2]_{x=x^{(t)}}$.

It should be noted that we increased the fixed ℓ_2 norm proportionally with sub-sampled image scale when taking an multiscaling scheme.

C. Overall Implementation

The overall algorithms is shown in Algorithms 2.

Algorithm 2 Blind Deconvolution (single-scaling version)

Input: blurry image y , kernel size $L, \lambda, \eta, \tau, IterMax$
Output: clear image x and degradation kernel k

```

1:  $y \leftarrow [\nabla_h y, \nabla_v y]$ 
2: Initializing  $x \leftarrow y$ 
3: Initializing  $k$  with an  $L \times L$  zero matrix adding [0.5 0.5]
   in the center
4: for  $t \leftarrow 1$  to  $IterMax$  do
5:   Updating  $x$  using Algorithm 3 in [8]
6:   Updating  $k$  using Algorithm 1
7: end for
8:  $x \leftarrow$  Non-blind deconvolution on  $k$  and  $y$ 

```

We implement these algorithms on the derivative field of x and y based on the fact that

$$\nabla(x \circ k) = \nabla x \circ k. \tag{33}$$

Kernels in our implementation are forced squares. We applied the non-blind deconvolution method in [20].

V. EXPERIMENTS AND RESULTS

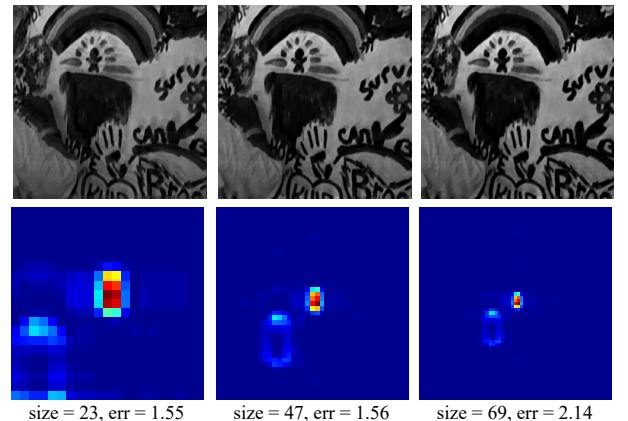


Fig. 8. Deblurring results using low-rank regularization.

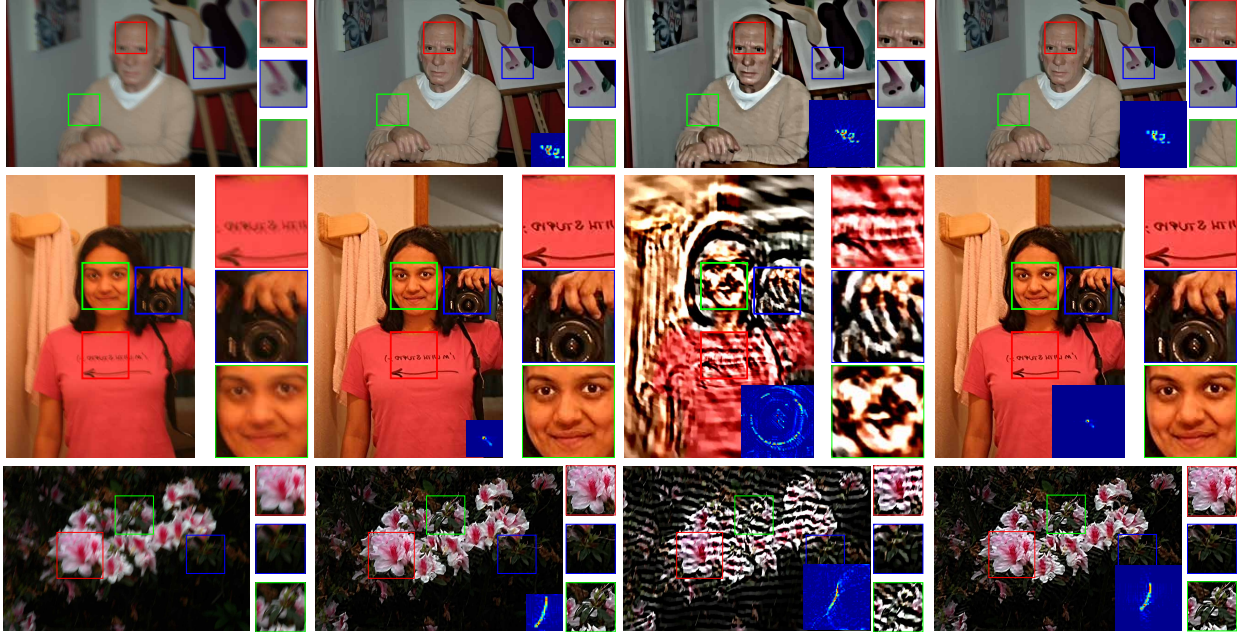


Fig. 9. Tests on real-world images. From left to right: the blurry images, 31×31 kernel with low-rank, 61×61 without low-rank and 61×61 with low-rank.

In response to high error ratios of large kernels mentioned in Figure 1 and to show the efficiency of our regularization, we used the same parameters except μ and σ in Figure 1. Figure 8 shows low-rank regularized kernels are much more robust to kernel size. Noises in kernels are efficiently reduced and qualities of restored images are enhanced.

We also tested our implementation on real-world images and compared the results with and without using low-rank regularization (See Figure 9). Restored images without using low-rank regularization look muddy for strong noise in estimated kernels. In contrast, regularized kernels are much cleaner, and qualities of restored images match those restored by small kernels.

It should be noted here that in experiments of Figure 8 and Figure 9, we deliberately omitted multi-scaling scheme and threshold to expose the effectiveness of low-rank regularization itself. Those operations may also reduce the large-kernel effect by sub-sampling and purifying the estimated kernel.

Our regularization method performs robust on larger kernels

upon dataset from [14]. Figure 10 shows the success rates of state-of-the-art methods versus our implementations with and without (set μ and σ zero) low-rank regularization. Parameters are fixed during the whole experiment, where $\sigma = 1$, $\mu = 1$, $\tau = 5 \times 10^{-5}$, $OuterIterMax = 20$, $CGIterMax = 3$ and $innerIterMax = 10$ and a 7-layer multi-scaling pyramid is taken. Low-rank regularization works more effectively than the regularization-free implementation and the state-of-art.

In addition, we test compared our implementation to several state-of-arts on a real-world image to reveal the robustness of our regularization on kernel sizes. Figure 11 shows that 185×185 size yields strong noises in estimated kernels of previous works (Cho & Lee, Krishnan *et al.*), and even changes main bodies of kernels (Krishnan *et al.*, Zuo *et al.*). Contrastively, our implementation can keep the kernel stable for the larger size.

Our implementation processed images of 255×255 pixels with truth blur sizes in 85 sec on average on a Lenovo ThinkCentre computer with Core i7 processor. Our MATLAB codes and deblurring results will be distributed after the present paper has been officially accepted for publication.

VI. CONCLUSION

In this paper, we demonstrate that kernel sizes larger than ground truth produce increased noises. We attribute the large-kernel effect to the *Plumping Effect*. We also take low-rank regularization and reduce the large-kernel effect efficiently. In practical implementations, even for noise-free y , the intermediate $\hat{x}^{(i)}$ is unlikely to iterate to truth, hence some parts of y will be treated as implicit noises, which may intensify the effect even more than expected.

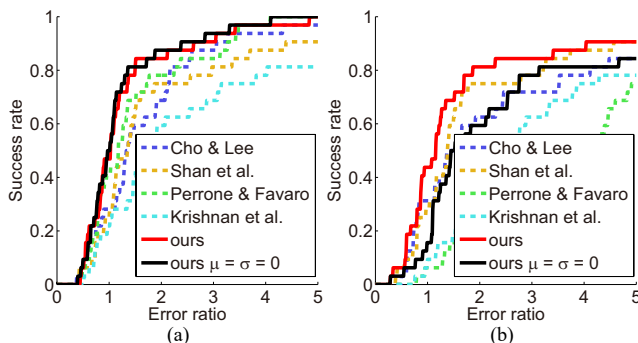


Fig. 10. Success rates. (a) Results on truth sizes. (b) Results on double sizes of the truth.

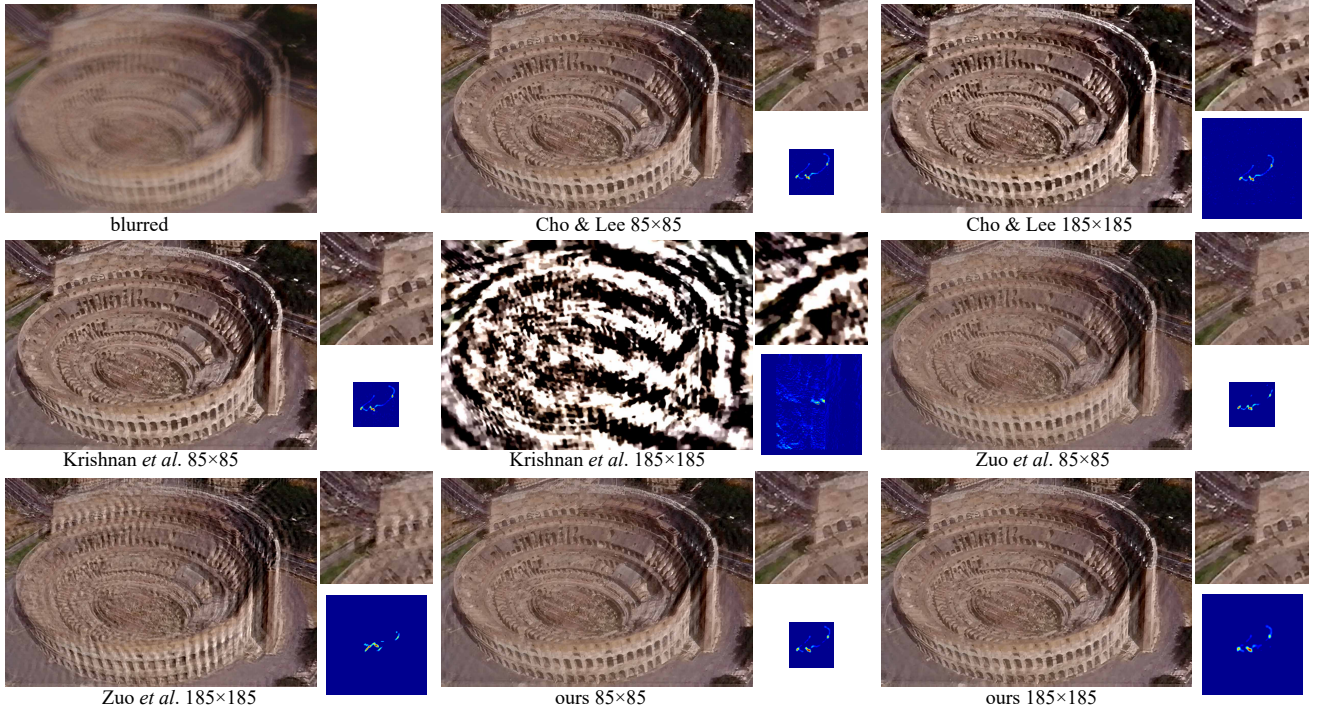


Fig. 11. Tests on a real-world image. It's recommended to zoom into estimated kernels to compare the cleanliness and main bodies of kernels.

APPENDIX

PROOF TO THEOREM 2

Assume M to be odd and $M = 2m + 1$ ($m \in \mathbb{N}^+$). Then,

$$T_{\mathbf{x}}(M) = \begin{bmatrix} x_{m+1} & \cdots & x_2 & x_1 & 0 & \cdots & 0 \\ \vdots & & \vdots & x_2 & x_1 & \ddots & \vdots \\ x_{M-1} & & \vdots & \vdots & x_2 & \ddots & 0 \\ x_M & \ddots & \vdots & \vdots & \vdots & \ddots & x_1 \\ 0 & \ddots & x_{M-1} & \vdots & \vdots & \ddots & x_2 \\ \vdots & \ddots & x_M & x_{M-1} & \vdots & & \vdots \\ 0 & \cdots & 0 & x_M & x_{M-1} & \cdots & x_{m+1} \end{bmatrix} \quad (34)$$

$$= \begin{bmatrix} J^{(-m)}\mathbf{x} & \cdots & J^{(-1)}\mathbf{x} & \mathbf{x} & J^{(1)}\mathbf{x} & \cdots & J^{(m)}\mathbf{x} \end{bmatrix}. \quad (35)$$

For any M -by- M matrix A , $\text{rank}(A) = M$ i.f.f. $\det(A) \neq 0$. Thus,

$$\Pr(\text{rank}(T_{\mathbf{x}}(M)) = M) = \Pr(\det(T_{\mathbf{x}}(M)) \neq 0). \quad (36)$$

As we know, the explicit formula of determinant of a Toeplitz matrix on its elements is unsolved in the current literature. Li [25] gives a concrete expression of $\det(T_{\mathbf{x}}(M))$ by using LU factorization but fails to fit all situations (e.g. when $x_{m+1} = 0$). However, it can be shown that $\det(T_{\mathbf{x}}(M))$ equals a multivariate polynomial function without manipulating the whole expression. By using Laplace expansion on

$\det(T_{\mathbf{x}}(M))$, the item of largest degree is x_{m+1}^M with factor 1.

Lemma. Let X be a continuous r.v. in the finite support domain $[a, b]$. Let $P : \mathbb{R} \rightarrow \mathbb{R}$ be a polynomial function

$$P(x) = x^k + Q(x)$$

where Q is a finite polynomial function with the largest degree less than k . Generate a new r.v.

$$Y = P(X).$$

Then, for $\forall y \in \mathbb{R}$, the Cumulative Distribution Function (CDF) F_Y is continuous at y .

Proof.

$$F_Y(y) = \Pr(Y \leq y) = \int_{\Xi(y)} f_X(x) dx$$

where $\Xi(y) = \{x | P(x) \leq y, x \in \mathbb{R}\}$.

For $\forall y \in \mathbb{R}$,

$$\Xi(y^+) = \Xi(y)$$

and

$$\Xi(y^-) = \Xi(y) \setminus \Omega(y)$$

where $\Omega(y) = \{x | P(x) - y = 0\}$.

Based on Beppo Levi's Theorem,

$$\lim_{\xi \rightarrow y^+} \int_{\Xi(\xi)} f_X(x) dx = \int_{\Xi(y)} f_X(x) dx.$$

Because $P(x) \neq c$ (c is a constant), for $\forall y \in \mathbb{R}$, zeros of $P(x) - y$ are finite, hence the Lebesgue measure of $\Omega(y)$ is zero. We have

$$\lim_{\xi \rightarrow y^-} \int_{\Xi(\xi)} f_X(x) dx = \int_{\Xi(y)} f_X(x) dx.$$

Thus

$$F_Y(y^+) = F_Y(y^-) = F(y).$$

□

Theorem. Let X be a continuous r.v. with PDF

$$f_X(x) = \begin{cases} \beta \exp(-\gamma|x|^\alpha) & x \in [-1, 1] \\ 0 & \text{otherwise.} \end{cases}$$

For a sample of independent observations X_1, \dots, X_M , generate a new r.v.

$$Z = \det \begin{bmatrix} X_{m+1} & \cdots & X_2 & X_1 & 0 & \cdots & 0 \\ \vdots & & \vdots & X_2 & X_1 & \ddots & \vdots \\ X_{M-1} & & \vdots & \vdots & X_2 & \ddots & 0 \\ X_M & \ddots & \vdots & \vdots & \vdots & \ddots & X_1 \\ 0 & \ddots & X_{M-1} & \vdots & \vdots & & X_2 \\ \vdots & \ddots & X_M & X_{M-1} & \vdots & & \vdots \\ 0 & \cdots & 0 & X_M & X_{M-1} & \cdots & X_{m+1} \end{bmatrix}.$$

Then,

$$\Pr(Z = 0) = 0.$$

Proof. Based on the Law of Total Probability and Dominated Convergence Theorem,

$$\begin{aligned} & \Pr(Z = 0) \\ &= F_Z(0) - F_Z(0^-) \\ &= \int_{-\infty}^{\infty} \cdots \int_{-\infty}^{\infty} \int_{-\infty}^{\infty} \cdots \int_{-\infty}^{\infty} F_{Y(\xi_1, \dots, \xi_m, \xi_{m+2}, \dots, \xi_M)}(0) \\ & \quad f_X(\xi_1) \cdots f_X(\xi_m) f_X(\xi_{m+2}) \cdots f_X(\xi_M) \\ & \quad d\xi_1 \cdots d\xi_m d\xi_{m+2} \cdots d\xi_M \\ &- \lim_{z \rightarrow 0^-} \int_{-\infty}^{\infty} \cdots \int_{-\infty}^{\infty} \int_{-\infty}^{\infty} \cdots \int_{-\infty}^{\infty} F_{Y(\xi_1, \dots, \xi_m, \xi_{m+2}, \dots, \xi_M)}(z) \\ & \quad f_X(\xi_1) \cdots f_X(\xi_m) f_X(\xi_{m+2}) \cdots f_X(\xi_M) \\ & \quad d\xi_1 \cdots d\xi_m d\xi_{m+2} \cdots d\xi_M \\ &= \int_{-\infty}^{\infty} \cdots \int_{-\infty}^{\infty} \int_{-\infty}^{\infty} \cdots \int_{-\infty}^{\infty} (F_{Y(\xi_1, \dots, \xi_m, \xi_{m+2}, \dots, \xi_M)}(0) \\ & \quad - F_{Y(\xi_1, \dots, \xi_m, \xi_{m+2}, \dots, \xi_M)}(0^-)) f_X(\xi_1) \cdots f_X(\xi_m) \\ & \quad f_X(\xi_{m+2}) \cdots f_X(\xi_M) d\xi_1 \cdots d\xi_m d\xi_{m+2} \cdots d\xi_M \end{aligned}$$

where

$$\begin{aligned} & Y(\xi_1, \dots, \xi_m, \xi_{m+2}, \xi_M) \\ &= \det \begin{bmatrix} X_{m+1} & \cdots & \xi_2 & \xi_1 & 0 & \cdots & 0 \\ \vdots & & \vdots & \xi_2 & \xi_1 & \ddots & \vdots \\ \xi_{M-1} & & \vdots & \vdots & \xi_2 & \ddots & 0 \\ \xi_M & \ddots & \vdots & \vdots & \vdots & \ddots & \xi_1 \\ 0 & \ddots & \xi_{M-1} & \vdots & \vdots & & \xi_2 \\ \vdots & \ddots & \xi_M & \xi_{M-1} & \vdots & & \vdots \\ 0 & \cdots & 0 & \xi_M & \xi_{M-1} & \cdots & X_{m+1} \end{bmatrix} \\ &= X_{m+1}^M + Q_{\xi_1, \dots, \xi_m, \xi_{m+2}, \dots, \xi_M}(X_{m+1}). \end{aligned}$$

$Q_{\xi_1, \dots, \xi_m, \xi_{m+2}, \dots, \xi_M}$ is a polynomial function with the largest degree less than M . Based on Lemma, we have

$$F_{Y(\xi_1, \dots, \xi_m, \xi_{m+2}, \dots, \xi_M)}(0) - F_{Y(\xi_1, \dots, \xi_m, \xi_{m+2}, \dots, \xi_M)}(0^-) = 0.$$

Hence,

$$\Pr(Z = 0) = 0.$$

□

ACKNOWLEDGMENT

Li Si-Yao thank Dongwei Ren for his generous guidance and constructive conversations.

We thank Junfeng Li, Yongjian Hu and Wenyi Zeng for their suggestions and inspirations on the proof to Theorem 2.

REFERENCES

- [1] T. F. Chan and C.-K. Wong, "Total variation blind deconvolution," *IEEE Trans. Image Process.*, vol. 7, no. 3, pp. 370–375, 1998.
- [2] R. Fergus, B. Singh, A. Hertzmann, S. T. Roweis, and W. T. Freeman, "Removing camera shake from a single photograph," in *ACM Trans. Graph.*, vol. 25, no. 3, 2006, pp. 787–794.
- [3] S. Cho and S. Lee, "Convergence analysis of map based blur kernel estimation," *arXiv preprint arXiv:1611.07752*, 2016.
- [4] L. Xu and J. Jia, "Two-phase kernel estimation for robust motion deblurring," in *Proc. ECCV*, 2010, pp. 157–170.
- [5] D. Gong, M. Tan, Y. Zhang, A. Van den Hengel, and Q. Shi, "Blind image deconvolution by automatic gradient activation," in *Proc. CVPR*, 2016, pp. 1827–1836.
- [6] S. Cho and S. Lee, "Fast motion deblurring," *ACM Trans. Graph.*, vol. 28, no. 5, p. 145, 2009.
- [7] L. Xu, S. Zheng, and J. Jia, "Unnatural l0 sparse representation for natural image deblurring," in *Proc. CVPR*, 2013, pp. 1107–1114.
- [8] D. Krishnan, T. Tay, and R. Fergus, "Blind deconvolution using a normalized sparsity measure," in *Proc. CVPR*, 2011, pp. 233–240.
- [9] Q. Shan, J. Jia, and A. Agarwala, "High-quality motion deblurring from a single image," *ACM Trans. Graph.*, vol. 27, no. 3, p. 73, 2008.
- [10] J. Pan, Z. Lin, Z. Su, and M.-H. Yang, "Robust kernel estimation with outliers handling for image deblurring," in *Proc. CVPR*, 2016, pp. 2800–2808.
- [11] W. Zuo, D. Ren, S. Gu, L. Lin, and L. Zhang, "Discriminative learning of iteration-wise priors for blind deconvolution," in *Proc. CVPR*, 2015, pp. 3232–3240.
- [12] D. Perrone and P. Favaro, "Total variation blind deconvolution: The devil is in the details," in *Proc. CVPR*, 2014, pp. 2909–2916.
- [13] D. Kundur and D. Hatzinakos, "Blind image deconvolution," *IEEE Signal Processing Mag.*, vol. 13, no. 3, pp. 43–64, 1996.
- [14] A. Levin, Y. Weiss, F. Durand, and W. T. Freeman, "Understanding and evaluating blind deconvolution algorithms," in *Proc. CVPR*, 2009, pp. 1964–1971.
- [15] H. C. Andrews and B. R. Hunt, *Digital image restoration*. Englewood Cliffs, NJ: Prentice-Hall, 1977, ch. 5.2, pp. 102–103.

- [16] R. M. Gray, "Toeplitz and circulant matrices: A review," *Foundations and Trends in Communication and Information Theory*, vol. 2, no. 3, pp. 155–239, 2006.
- [17] E. Kaltofen and A. Lobo, "On rank properties of toeplitz matrices over finite fields," in *Proc. Int. Symp. Symbolic and Algebraic Computation (ISSAC)*, 1996, pp. 241–249.
- [18] B. A. Olshausen and D. J. Field, "Emergence of simple-cell receptive field properties by learning a sparse code for natural images," *Nature*, vol. 381, no. 6583, p. 607, 1996.
- [19] Y. Weiss and W. T. Freeman, "What makes a good model of natural images?" in *Proc. CVPR*, 2007, pp. 1–8.
- [20] D. Krishnan and R. Fergus, "Fast image deconvolution using hyper-laplacian priors," in *Proc. NIPS*, 2009, pp. 1033–1041.
- [21] D. Spielman, "Lecture 2: The condition number," *MIT OpenCourseWare: Behavior of Algorithms*, vol. 1, no. 2, p. 3, 2002.
- [22] —, "Lecture 3: The largest singular value of a matrix," *MIT OpenCourseWare: Behavior of Algorithms*, vol. 1, no. 1, p. 1, 2002.
- [23] M. Fazel, H. Hindi, and S. P. Boyd, "Log-det heuristic for matrix rank minimization with applications to hankel and euclidean distance matrices," in *Proc. American Control Conf. (ACC)*, vol. 3, 2003, pp. 2156–2162.
- [24] W. Dong, G. Shi, X. Li, Y. Ma, and F. Huang, "Compressive sensing via nonlocal low-rank regularization," *IEEE Trans. Image Process.*, vol. 23, no. 8, pp. 3618–3632, 2014.
- [25] H. Li, "On calculating the determinants of toeplitz matrices," *J. Appl. Math. Bioinformatics*, vol. 1, no. 1, p. 55, 2011.



Ping Guo (SM'05) received his B.Sc. degree and M.Sc. degree in optics from Peking University in 1980 and 1983 respectively, and the Ph.D degree in computer science from The Chinese University of Hong Kong in 2001.

From 1993 to 1994 he was with the Department of Computer Science and Engineering at Wright State University as a visiting faculty. From May to August 2000 he was with the National Laboratory of Pattern Recognition at Chinese Academy of Sciences as a research associate. From July to December 2005 he was with the Computer Science Department at The Chinese University of Hong Kong as a research associate. He is currently a Professor with the School of Systems Science at Beijing Normal University, and also a Professor with the School of Computer Science and Technology at Beijing Institute of Technology. He has authored over 260 papers in important academic journals and conferences, including AAAI, the *International Joint Conference on Neural Networks*, the *IEEE TRANSACTIONS ON SYSTEMS, MAN, AND CYBERNETICS: SYSTEMS* and the *IEEE TRANSACTIONS ON NEURAL NETWORKS*. His current research interests include computational intelligence application on image processing, pattern recognition, software reliability engineering, optical computing and spectral analysis.



Li Si-Yao received the B.Sc. degree in computer science from Beijing Normal University, Beijing, China, in 2016. He is currently pursuing the M.E. degree in computer science at Beijing Normal University. His research interest includes computer vision and neural networks.



Qian Yin received her Ph.D in mathematic from Beijing Normal University in 2006. She is currently an Associate Professor in College of Information Science and Technology, and the director of Image Processing and Pattern Recognition Laboratory in Beijing Normal University. Her current research interest includes low-level vision and intelligent processing of astronomical data.